



ARTICLE

High Accuracy Simulation of Electro-Thermal Flow for Non-Newtonian Fluids in BioMEMS Applications

Umer Farooq¹, Nabil Kerdid^{2,*}, Yasir Nawaz³ and Muhammad Shoaib Arif⁴

¹College of Mathematical Sciences, Harbin Engineering University, Harbin City, 150001, China

²Department of Mathematics and Statistics, College of Science, Imam Mohammad Ibn Saud Islamic University (IMSIU), P.O. Box 90950, Riyadh, 11623, Saudi Arabia

³Department of Mathematics, Air University, PAF Complex E-9, Islamabad, 44000, Pakistan

⁴Department of Mathematics and Sciences, College of Humanities and Sciences, Prince Sultan University, Riyadh, 11586, Saudi Arabia

*Corresponding Author: Nabil Kerdid. Email: nmkerdid@imamu.edu.sa

Received: 17 April 2025; Accepted: 02 July 2025; Published: 31 July 2025

ABSTRACT: In this study, we proposed a numerical technique for solving time-dependent partial differential equations that arise in the electro-osmotic flow of Carreau fluid across a stationary plate based on a modified exponential integrator. The scheme is comprised of two explicit stages. One is the exponential integrator type stage, and the second is the Runge-Kutta type stage. The spatial-dependent terms are discretized using the compact technique. The compact scheme can achieve fourth or sixth-order spatial accuracy, while the proposed scheme attains second-order temporal accuracy. Also, a mathematical model for the electro-osmotic flow of Carreau fluid over the stationary sheet is presented with heat and mass transfer effects. The governing equations are transformed into dimensionless partial differential equations and solved by the proposed scheme. Simulation results reveal that increasing the Helmholtz–Smoluchowski velocity U_{HS} by 400% leads to a 60%–75% rise in peak flow velocity, while the electro-osmotic parameter m_e enhances near-wall acceleration. Conversely, velocity decreases significantly with higher Weissenberg numbers, indicating the Carreau fluid’s elastic resistance and increased magnetic field strength due to improved Lorentz forces. Temperature rises with the thermal conductivity parameter ϵ_2 , while higher reaction rates γ diminish concentration and local Sherwood number values. The simulation findings show the scheme’s correctness and efficacy in capturing the complicated interactions in non-Newtonian electro-osmotic transport by revealing the notable impact of electrokinetic factors on flow behaviour. The proposed model is particularly relevant for Biological Micro-Electro-Mechanical Systems (BioMEMS) applications, where precise control of electro-thermal transport in non-Newtonian fluids is critical for lab-on-a-chip diagnostics, drug delivery, and micro-scale thermal management.

KEYWORDS: Modified exponential integrator; stability; convergence; carreau fluid: electro-osmosis flow; BioMEMS applications

1 Introduction

Numerical methods play a vital role in solving differential equations, which are essential because some physical phenomena can be expressed as differential equations. Ordinary and partial differential equations are the two main types of differential equations. One independent variable makes up ordinary differential equations, while two or more independent variables are involved in partial differential equations. So, ordinary differential equations are one way of discretization, but partial differential equations require more



than one way of discretization. Some differential equations exist that contain time-dependent terms. So, these time-dependent terms are approximated by numerical schemes. There exist two types of numerical schemes. Among these, some schemes are explicit, and others are implicit categories. The explicit scheme does not require linearization of the non-linear terms in differential equations, but the implicit schemes require linearization. Also, one additional iterative scheme can be used to solve difference equations discretized by the implicit schemes. However, some implicit schemes are unconditionally stable so that any step length can be used, but primarily explicit schemes are conditionally stable, so they have restrictions on step size. If appropriate step length is chosen for explicit schemes, the stable solution can be obtained; otherwise, the solution will diverge if the step size or involved parameter in the given differential equation does not meet the stability condition. If the finite difference schemes do space discretization, a stability analysis, called Fourier series analysis, exists to find the stability condition. Fourier series analysis can be employed for both explicit and implicit schemes. It gives an exact stability condition for linear differential equations but estimates the exact stability condition for non-linear differential equations. Also, explicit and implicit schemes are divided into multi-step or multi-stage schemes. Multi-stage Runge-Kutta-type schemes require information at a one-time level to find the solution at the next time level. These methods contain one or more predictor stages and one corrector stage.

The process known as electro-osmosis occurs when an electric field causes fluid to flow through a porous substance or across a surface. It happens when a fluid in contact with a charged surface is exposed to an electric field, which causes the fluid to move in reaction to the electric force. The boundary between a solid and a fluid causes the formation of an electric double layer. This layer comprises a Stern layer of adsorbed ions and a diffuse counter-ion layer in the fluid. When an electric field is generated perpendicular to the surface, the charged particles in the fluid move toward the electrodes, dragging the bulk fluid with them. Electro-osmotic flow is the term for the fluid flow produced by this movement. Electro-osmosis is a flexible and effective method for controlling fluid flow in various applications by utilizing the interaction between electric fields and charged surfaces or particles.

The presence of ions in viscoelastic liquids causes the generation of electric Coulomb forces, which exert an electric field on the ions [1]. Electro-osmosis efficiently modifies and regulates blood flow and structure [2]. Levine et al. [3] and the team conducted some of the earliest theoretical investigations in electrokinetic rheology. Misra et al. [4] conducted a theoretical investigation examining how electro-osmotic forces affected the flow of micropolar liquids through a vibrating tiny conduit. Regarding blood rheology, Jubery looked into the physical consequences of electrokinetic events [5]. The effects of an electric field on electro-osmotic flow across a T-junction were investigated by Dutta et al. [6].

Both Jeffrey [7] in 1915 and Hamel [8] in 2009 were the first to find an exact solution to the problem of the constant flow of an incompressible fluid inside two intersecting planes with a converging-diverging character. The two-dimensional flow of Newtonian and non-Newtonian fluids of the Jeffrey-Hamel type via an inclined wall channel has been the subject of numerous investigations since then. The constant two-dimensional Jeffrey-Hamel nanofluid flow in a non-Darcy permeable medium was investigated in [9], along with the thermal leap and changing fluid properties. With an oblique magnetic ground, variable thermal conductivity, heat sink/source influences, and two collateral sheets, Dinarvand et al. [10] computationally investigated the aqueous $\text{Fe}_3\text{O}_4/\text{CNTs}$ binary nanofluid flow. Scholarly literature such as Garimella et al. [11], Harley et al. [12], etc., extensively details the Jeffery-Hamel flow in convergent-diverging channels, which is fundamental for Newtonian and non-Newtonian fluids. PJ developed the non-Newtonian fluid model. Carreau [13] provides a more comprehensive explanation of the properties of materials whose viscosity is affected by the shear rate. This model effectively depicts the thickening and thinning properties at different shear speeds.

Regarding Carreau nanofluid flow, Khan and Ali Shehzad investigate the effects of microstructure on the oscillating and periodically shifting configuration [14]. Akbar and Nadeem has utilized the Carreau fluid model to represent blood flow via a narrowing, stenotic artery [15]. Recent efforts have explored electro-osmotic transport in Carreau fluids using advanced numerical techniques to capture the non-linear rheological and electrokinetic behaviour under microchannel confinement [16]. The influence of stochastic fluctuations and porous medium resistance on electro-osmotic flow has also been investigated, revealing the critical role of random perturbations and energy dissipation in shaping transport behaviour in microfluidic systems [17]. According to Hayat et al. [18], non-Newtonian fluids have extraordinarily complex constitutive equations, increasing the number of terms and governing equation order. A numerical investigation on the steady incompressible laminar two-dimensional hybrid nanofluid flow upon a convectively warmed moving wedge with radiative transition has been carried out by Berrehal et al. [19] based on the Carreau model of blood viscosity, which is a non-linear model concerning shear rate. For the flow in circular pipes and thin slits, Sochi [20] used two separate fluids, the Carreau, and the Cross fluids, to study the analytical solutions. About Taylor's famous paint scraping problem, which provides a model for studying wall-driven corner flow caused by an oblique plane moving at a constant speed, Chaffin and Rees [21] studied the behaviour of the inertia-less limit of a Carreau fluid in this kind of system. Recent research has investigated electro-osmotic flow in complicated shapes and viscoelastic fluids. For example, the work by [22] looks at electro-osmotic peristaltic streaming of a fractional second-grade viscoelastic nanofluid with carbon nanotubes in a ciliated tube. This shows how electrokinetics and non-Newtonian behaviour interact in fractional-order modelling frameworks. Using fractional viscoelastic models, researchers have looked at electro-osmotic transport in non-Newtonian fluids [23]. Most of these works are around peristaltic movements and certain shapes.

In contrast, our study looks at the electro-thermal flow of Carreau fluids with full Multiphysics coupling, which is important for BioMEMS applications. Researchers have also investigated magnetized non-Newtonian nanofluids in biomedical settings. For example, the study in [24] did a thermal analysis of blood-based nanofluid flow with a couple of stresses in a vertical microchannel under magnetic effects. This showed how the interaction of the magnetic field and the microstructural fluid behaviour affected temperature regulation, an important factor for thermal control in bio-microdevices. In other studies, optimization methods have been used on complicated non-Newtonian models. For instance, the study in [25] used response surface methodology to optimize the flow of Eyring–Powell fluids with Cattaneo–Christov heat flux and cross-diffusion effects. This shows how advanced thermal models can be combined with transport phenomena to give precise control in non-linear fluid systems.

In this paper, we proposed a modified exponential integrator-based numerical method for solving time-dependent partial differential equations generated in the electro-osmotic flow of Carreau fluid over a stationary plate. Comprising two explicit phases, the suggested method is: the first uses an exponential time integrator to manage stiff linear components; the second uses a Runge-Kutta-type technique to capture the non-linear dynamics. We use a compact finite difference method that can provide fourth- or sixth-order accuracy to improve spatial accuracy. This hybrid computing system performs strongly in stiff, non-linear domains and second-order time precision. Electric potential, Helmholtz-Smoluchowski velocity, and thermodiffusive forces' influences are included to create the mathematical formulation of the EOF problem. Using the suggested method, the governing equations are non-dimensionalized and solved numerically. The simulation findings show the notable impact of electrokinetic factors on flow behaviour, proving the scheme's correctness and efficiency in capturing the intricate interactions in non-Newtonian electro-osmotic transport. In this paper, we make the following contributions.

1. We develop a modified two-stage explicit exponential integrator combining exponential and Runge-Kutta techniques for solving non-linear time-dependent PDEs.

2. We incorporate a high-order compact finite difference scheme to enhance spatial accuracy, achieving fourth/sixth-order precision.
3. We model the electro-osmotic flow of Carreau fluid with integrated effects of magnetic field, porous media, heat, and mass transfer.
4. We captured the influence of variable thermal conductivity and reaction kinetics on flow, temperature, and concentration profiles.
5. We analyze oscillatory boundary conditions, demonstrating their impact on electrokinetic transport and thermal diffusion. The study provides a detailed parametric investigation (e.g., W_e , M , $F_s m_e$, γ) and their influence on velocity, temperature, and concentration, which has direct implications for the design and tuning of BioMEMS and microfluidic devices where precision control is crucial.
6. We verify that the system may address complicated fluid behavior without linearization or iterative solvers by maintaining nonlinearity.

The rest of the paper is organized as follows. [Section 2](#) constructs the numerical scheme for solving time-dependent partial differential equations generated in the electro-osmotic flow of Carreau fluid over a stationary plate. [Section 3](#) presents a stability analysis for the proposed scheme. [Section 4](#) presents a problem formulation of the electro-osmotic flow of the Carreau fluid model across a stationary plate. Empirical results are provided in [Section 5](#). [Section 6](#) concludes the paper.

2 Proposed Exponential Time Integrator Scheme

An explicit predictor-corrector scheme is proposed for solving time-dependent partial differential equations. The first stage of the scheme is the predictor stage, while the second stage of the scheme is called the corrector stage. The whole domain is divided into small parts to apply the scheme. First, the solution is found at an arbitrary time level, and then the actual solution will be found at the next time level. For constructing the scheme, consider the following time-dependent partial differential equation.

$$\frac{\partial p}{\partial t} = F \left(p, \frac{\partial p}{\partial x}, \frac{\partial p}{\partial y}, \frac{\partial^2 p}{\partial y^2} \right) \quad (1)$$

and initial and boundary conditions are given as:

$$p(0, x, y) = f_1(x, y), p(t, 0, y) = f_2(t, y), p(t, x, 0) = f_3(t, x), p(t, x, L) = f_4(t, x)$$

where L is a finite number and f_i 's are functions of spatial and temporal coordinates.

2.1 Reformulation for Exponential Integrator

For constructing the scheme, [Eq. \(1\)](#) can be written as:

$$\frac{\partial p}{\partial t} = -2p + P \quad (2)$$

where $P = F + 2p$. This allows the linear part $-2p$ to be handled by exponential integration.

2.2 Predictor Stage

The predictor or first stage of the scheme can be written as:

$$\bar{p}_{l,m}^{n+1} = p_{l,m}^n e^{-2\Delta t} + \frac{(-e^{-2\Delta t} + 1)}{2} P_{l,m}^n \quad (3)$$

where Δt is temporal step size and $P_{l,m}^n = F\left(p_{l,m}^n, \frac{\partial p}{\partial x}\Big|_{l,m}^n, \frac{\partial p}{\partial y}\Big|_{l,m}^n, \frac{\partial^2 p}{\partial y^2}\Big|_{l,m}^n\right) + 2p_{l,m}^n$. We use an exponential integrator to estimate an intermediate solution $\bar{p}_{l,m}^{n+1}$ at the next time level. This gives a prediction of the solution using known quantities at time level n .

2.3 Corrector Stage

The second stage, or corrector stage of the scheme, contains three parameters whose values will be computed by matching terms of the Taylor series expansion of the equation given by:

$$p_{l,m}^{n+1} = ap_{l,m}^n + b\bar{p}_{l,m}^{n+1} + c(e^{\Delta t} - 1)F(\bar{p}_{l,m}^{n+1}) \tag{4}$$

The constants a, b, c are determined using Taylor series expansion to ensure second-order accuracy in time.

Rewrite Eqs. (3) and (4) as:

$$\bar{p}_{l,m}^{n+1} = p_{l,m}^n e^{-2\Delta t} + \frac{(-e^{-2\Delta t} + 1)}{2} \left\{ \frac{\partial p}{\partial t}\Big|_{l,m}^n + 2p_{l,m}^n \right\} = p_{l,m}^n + \frac{(-e^{-2\Delta t} + 1)}{2} \frac{\partial p}{\partial t}\Big|_{l,m}^n \tag{5}$$

$$p_{l,m}^{n+1} = ap_{l,m}^n + b\bar{p}_{l,m}^{n+1} + c(e^{\Delta t} - 1) \frac{\partial \bar{p}}{\partial t}\Big|_{l,m}^{n+1} \tag{6}$$

Expanding $p_{i,j}^{n+1}$ using Taylor series expansion as:

$$p_{l,m}^{n+1} = p_{l,m}^n + \Delta t \frac{\partial p}{\partial t}\Big|_{l,m}^n + \frac{(\Delta t)^2}{2} \frac{\partial^2 p}{\partial t^2}\Big|_{l,m}^n + O((\Delta t)^3) \tag{7}$$

By putting Eqs. (5) and (7) into Eq. (6).

$$p_{l,m}^n + \Delta t \frac{\partial p}{\partial t}\Big|_{l,m}^n + \frac{(\Delta t)^2}{2} \frac{\partial^2 p}{\partial t^2}\Big|_{l,m}^n = ap_{l,m}^n + b\left(p_{l,m}^n + \frac{(-e^{-2\Delta t} + 1)}{2} \left(\frac{\partial p}{\partial t}\Big|_{l,m}^n\right)\right) + c(e^{\Delta t} - 1) \left\{ z \frac{\partial p}{\partial t}\Big|_{l,m}^n + \frac{(-e^{-2\Delta t} + 1)}{2} \left(\frac{\partial^2 p}{\partial t^2}\Big|_{l,m}^n\right) \right\} \tag{8}$$

By equating coefficients of $p_{l,m}^n, \frac{\partial p}{\partial t}\Big|_{l,m}^n$ and $\frac{\partial^2 p}{\partial t^2}\Big|_{l,m}^n$ on both sides of Eq. (8) to yield.

$$\Delta t = \frac{1 = a + b}{\frac{b(-e^{-2\Delta t} + 1)}{2} + c(e^{\Delta t} - 1)} \left. \begin{array}{l} \\ \frac{(\Delta t)^2}{2} = c(e^{\Delta t} - 1) \frac{(-e^{-2\Delta t} + 1)}{2} \end{array} \right\} \tag{9}$$

By solving a system of linear Eq. (9) the values for a , b and c are:

$$\left. \begin{aligned} a &= \frac{(1 - e^{-2\Delta t})(1 - e^{-2\Delta t} - 2\Delta t) + 2(\Delta t)^2}{(1 - e^{-2\Delta t})^2} \\ b &= \frac{2\Delta t(1 - e^{-2\Delta t} - \Delta t)}{(1 - e^{-2\Delta t})^2} \\ c &= \frac{(\Delta t)^2}{(1 - e^{-2\Delta t})(e^{\Delta t} - 1)} \end{aligned} \right\} \quad (10)$$

2.4 Spatial Derivative Approximation

Let $F = a_1 p + a_2 \frac{\partial p}{\partial x} + a_3 \frac{\partial p}{\partial y} + a_4 \frac{\partial^2 p}{\partial y^2}$ in Eq. (1), then the first and second stages of the proposed scheme can be expressed as:

$$\bar{p}_{l,m}^{n+1} = p_{l,m}^n + \left(\frac{-e^{-2\Delta t} + 1}{2} \right) \left\{ a_1 p_{l,m}^n + a_2 \left. \frac{\partial p}{\partial x} \right|_{l,m}^n + a_3 \left. \frac{\partial p}{\partial y} \right|_{l,m}^n + a_4 \left. \frac{\partial^2 p}{\partial y^2} \right|_{l,m}^n \right\} \quad (11)$$

$$p_{l,m}^{n+1} = a p_{l,m}^n + b \bar{p}_{l,m}^{n+1} + c (e^{\Delta t} - 1) \left\{ a_1 \bar{p}_{l,m}^{n+1} + a_2 \left. \frac{\partial \bar{p}}{\partial x} \right|_{l,m}^{n+1} + a_3 \left. \frac{\partial \bar{p}}{\partial y} \right|_{l,m}^{n+1} + a_4 \left. \frac{\partial^2 \bar{p}}{\partial y^2} \right|_{l,m}^{n+1} \right\} \quad (12)$$

So far in this work, a time discretizing scheme is constructed, and now a space discretizing scheme is applied to Eq. (1). We use high-order compact finite difference schemes for spatial derivatives: First derivative in x : matrix form via $M_1^{-1}N_1$, First derivative in y : matrix form via $M_2^{-1}N_2$ and Second derivative in y : matrix form via $M_3^{-1}N_3$.

2.5 Final Predictor-Corrector Form (Matrix-Based)

To implement the space discretizing scheme, matrices are provided as:

$$\bar{p}_{l,m}^{n+1} = p_{l,m}^n + \left(\frac{-e^{-2\Delta t} + 1}{2} \right) [a_1 p_{l,m}^n + a_2 M_1^{-1} N_1 p_{l,m}^n + a_3 M_2^{-1} N_2 p_{l,m}^n + a_4 M_3^{-1} N_3 p_{l,m}^n] \quad (13)$$

$$p_{l,m}^{n+1} = a p_{l,m}^n + b \bar{p}_{l,m}^{n+1} + c (e^{\Delta t} - 1) [a_1 \bar{p}_{l,m}^{n+1} + a_2 M_1^{-1} N_1 \bar{p}_{l,m}^{n+1} + a_3 M_2^{-1} N_2 \bar{p}_{l,m}^{n+1} + a_4 M_3^{-1} N_3 \bar{p}_{l,m}^{n+1}] \quad (14)$$

where M_i 's and N_i 's are matrices generated by the coefficients of the left- and right-hand sides of the following equations.

$$\beta_1 p'_{l-1,m} + p'_{l,m} + \beta_1 p'_{l+1,m} = c_0 \frac{(p_{l+1,m}^n - p_{l-1,m}^n)}{2\Delta x} + c_1 \frac{(p_{l+2,m}^n - p_{l-2,m}^n)}{4\Delta x} \quad (15)$$

$$\beta_1 p'_{l,m-1} + p'_{l,m} + \beta_1 p'_{l,m+1} = c_0 \frac{(p_{l,m+1}^n - p_{l,m-1}^n)}{2\Delta x} + c_1 \frac{(p_{l,m+2}^n - p_{l,m-2}^n)}{4\Delta x} \quad (16)$$

$$\beta_2 p''_{l,m-1} + p''_{l,m} + \beta_2 p''_{l,m+1} = c_2 \frac{(p_{l,m+1}^n - 2p_{l,m}^n + p_{l,m-1}^n)}{(\Delta x)^2} + c_3 \frac{(p_{l,m+2}^n - 2p_{l,m}^n + p_{l,m-2}^n)}{4(\Delta y)^2} \quad (17)$$

where $c_0 = 2/3(\beta_1 + 2)$, $c_1 = 1/3(4\beta_1 - 1)$, $c_2 = 4/3(1 - \beta_2)$, $c_3 = 1/3(10\beta_2 - 1)$.

The proposed methodology is an explicit two-stage predictor-corrector method designed to solve time-dependent partial differential equations with high accuracy and computational efficiency. While the second

stage improves the answer using a Runge-Kutta-type corrector, the first stage uses an exponential integrator to manage the stiff linear component of the governing equations efficiently. The method obtains second-order time precision using analytical determination of the weighting coefficients via Taylor series expansion. Compact finite difference approximations are used to provide high-order spatial accuracy; they can provide fourth- or sixth-order accuracy depending on the formulation. The method is also designed in matrix form for quick execution and scaling to more dimensional issues. Its clear character makes it especially appropriate for simulating non-linear and electrokinetically driven non-Newtonian flows, such as those modelled by the Carreau fluid under electro-osmotic circumstances with heat and mass transfer influences, since it removes the need for iterative solvers.

3 Stability Analysis

The Fourier series analysis serves as a criterion for determining the stability conditions of finite difference schemes. The study provides precise conditions for linear partial differential equations and assesses the stability conditions for non-linear differential equations. To employ this stability analysis, consider the following transformations.

$$M_1 e^{lI\psi_1+mI\psi_2} = \beta_1 e^{(l+1)I\psi_1+mI\psi_2} + e^{lI\psi_1+mI\psi_2} + \beta_1 e^{(l-1)I\psi_1+mI\psi_2} \tag{18}$$

$$N_1 e^{lI\psi_1+mI\psi_2} = c_o \frac{(e^{(l+1)I\psi_1+mI\psi_2} - e^{(l-1)I\psi_1+mI\psi_2})}{2\Delta x} + c_1 \frac{(e^{(l+2)I\psi_1+mI\psi_2} - e^{(l-2)I\psi_1+mI\psi_2})}{4\Delta x} \tag{19}$$

$$M_2 e^{lI\psi_1+mI\psi_2} = \beta_1 e^{lI\psi_1+(m+1)I\psi_2} + e^{lI\psi_1+mI\psi_2} + \beta_1 e^{lI\psi_1+(m-1)I\psi_2} \tag{20}$$

$$N_2 e^{lI\psi_1+mI\psi_2} = c_o \frac{(e^{lI\psi_1+(m+1)I\psi_2} - e^{lI\psi_1+(m-1)I\psi_2})}{2\Delta y} + c_1 \frac{(e^{lI\psi_1+(m+2)I\psi_2} - e^{lI\psi_1+(m-2)I\psi_2})}{4\Delta y} \tag{21}$$

$$M_3 e^{lI\psi_1+mI\psi_2} = \beta_2 e^{lI\psi_1+(m+1)I\psi_2} + e^{lI\psi_1+mI\psi_2} + \beta_2 e^{lI\psi_1+(m-1)I\psi_2} \tag{22}$$

$$N_3 e^{lI\psi_1+mI\psi_2} = c_2 \frac{(e^{lI\psi_1+(m+1)I\psi_2} - 2e^{lI\psi_1+mI\psi_2} + e^{lI\psi_1+(m-1)I\psi_2})}{(\Delta y)^2} + c_3 \frac{(e^{lI\psi_1+(m+2)I\psi_2} - 2e^{lI\psi_1+mI\psi_2} + e^{lI\psi_1+(m-2)I\psi_2})}{4(\Delta y)^2} \tag{23}$$

By employing transformations (18)–(23) into the scheme’s first stage and simplifying it.

$$\begin{aligned} \bar{p}_{l,m}^{n+1} = & p_{l,m}^n e^{-2\Delta t} + \left(\frac{-e^{-2\Delta t} + 1}{2}\right) \left\{ a_1 + a_2 \left(\frac{c_o I \sin \psi_1 + 2c_1 I \sin \psi_1}{2\Delta x (2\beta_1 \cos \psi_1 + 1)}\right) + a_3 \left(\frac{c_o I \sin \psi_2 + 2c_1 I \sin \psi_2}{2\Delta y (2\beta_1 \cos \psi_2 + 1)}\right) \right. \\ & \left. + a_4 \left(\frac{c_2 (\cos \varphi_2 - 1) + 2c_3 (\cos \varphi_2 - 1)}{(\Delta y)^2 (2\beta_2 \cos \psi_2 + 1)}\right) + 2 \right\} p_{l,m}^n \end{aligned} \tag{24}$$

Eq. (24) can be written as:

$$\bar{p}_{l,m}^{n+1} = (\gamma_1 + I\gamma_2) p_{l,m}^n \tag{25}$$

where $\gamma_1 = e^{-2\Delta t} + \left(\frac{-e^{-2\Delta t} + 1}{2}\right) \left\{ a_4 \left(\frac{c_2 (\cos \varphi_2 - 1) + 2c_3 (\cos \varphi_2 - 1)}{(\Delta y)^2 (2\gamma_2 \cos \varphi_2 + 1)}\right) + a_1 + 2 \right\}$ and $\beta_2 = \left(\frac{-e^{-2\Delta t} + 1}{2}\right) \left\{ a_2 \left(\frac{2c_o \sin \varphi_1 + c_1 \sin \varphi_1}{2\Delta x (2\gamma_1 \cos \varphi_1 + 1)}\right) + a_3 \left(\frac{2c_o \sin \varphi_2 + c_1 \sin \varphi_2}{2\Delta y (2\gamma_1 \cos \varphi_2 + 1)}\right) \right\}$.

Now employing the transformations (18)–(23) into second stage of scheme that results in:

$$p_{l,m}^{n+1} = ap_{l,m}^n + b\bar{p}_{l,m}^{n+1} + c(e^{\Delta t} - 1) \left[a_1 + a_2 \left(\frac{c_o I \sin \psi_1 + 2c_1 I \sin \psi_1}{2\Delta x (2\beta_1 \cos \psi_1 + 1)} \right) + a_3 \left(\frac{c_o I \sin \psi_2 + 2c_1 I \sin \psi_2}{2\Delta y (2\beta_1 \cos \psi_2 + 1)} \right) \right. \\ \left. + a_4 \left(\frac{c_2 (\cos \psi_2 - 1) + 2c_3 (\cos \psi_2 - 1)}{(\Delta y)^2 (2\beta_2 \cos \psi_2 + 1)} \right) \right] \bar{p}_{l,m}^{n+1} \quad (26)$$

By rewriting Eq. (26) as:

$$p_{l,m}^{n+1} = \gamma_3 p_{l,m}^n + (\gamma_4 + I\gamma_5) \bar{p}_{l,m}^{n+1} \quad (27)$$

where $\gamma_3 = a$

$$\gamma_5 = c(e^{\Delta t} - 1) \left\{ a_2 \left(\frac{c_o \sin \psi_1 + 2c_1 \sin \psi_1}{2\Delta x (2\beta_1 \cos \psi_1 + 1)} \right) + a_3 \left(\frac{c_o \sin \psi_2 + 2c_1 \sin \psi_2}{2\Delta y (2\beta_1 \cos \psi_2 + 1)} \right) \right\}$$

$$\gamma_4 = b + c(e^{\Delta t} - 1) \left\{ a_4 \left(\frac{c_2 (\cos \psi_2 - 1) + 2c_3 (\cos \psi_2 - 1)}{(\Delta y)^2 (2\beta_2 \cos \psi_2 + 1)} \right) + a_1 \right\}$$

By inserting Eq. (25) into Eq. (27) results in:

$$p_{l,m}^{n+1} = \gamma_3 p_{l,m}^n + (\gamma_4 + I\gamma_5) (\gamma_1 + I\gamma_2) p_{l,m}^n \quad (28)$$

Eq. (28) can be rewritten as:

$$p_{l,m}^{n+1} = (\gamma_6 + I\gamma_7) p_{l,m}^n$$

where $\gamma_6 = \gamma_3 + \gamma_4\gamma_1 - \gamma_5\gamma_2$, $\gamma_7 = \gamma_1\gamma_5 + \gamma_2\gamma_4$.

The amplification factor for this case can be written as:

$$\left| \frac{p_{l,m}^{n+1}}{p_{l,m}^n} \right|^2 \leq \gamma_6 + \gamma_7 \leq 1 \quad (29)$$

If the scheme meets condition (29), it will remain stable. The condition (29) can be satisfied by choosing temporal and spatial step size values and involved parameters in the given differential equations.

In this work, the proposed scheme solves the convection-diffusion system. To do so, consider the following matrix-vector equation.

$$\frac{\partial \mathbf{f}}{\partial t} = A_1 \frac{\partial \mathbf{f}}{\partial x} + A_2 \frac{\partial \mathbf{f}}{\partial y} + A_3 \frac{\partial \mathbf{f}}{\partial y^2} \quad (30)$$

where \mathbf{f} is a vector and A_i 's are matrices.

The spatial components in Eq. (30) are discretized utilizing a compact methodology, while the proposed method discretizes the time-dependent term.

$$\bar{\mathbf{f}}_{l,m}^{n+1} = \mathbf{f}_{l,m}^n e^{-2\Delta t} + \left(\frac{e^{-2\Delta t} - 1}{2} \right) [A_1 M_1^{-1} N_1 \mathbf{f}_{l,m}^n + A_2 M_2^{-1} N_2 \mathbf{f}_{l,m}^n + A_3 M_3^{-1} N_3 \mathbf{f}_{l,m}^n - 2\mathbf{f}_{l,m}^n] \quad (31)$$

$$\mathbf{f}_{l,m}^{n+1} = a\mathbf{f}_{l,m}^n + b\bar{\mathbf{f}}_{l,m}^{n+1} + c(e^{\Delta t} - 1) [A_1 M_1^{-1} N_1 \bar{\mathbf{f}}_{l,m}^{n+1} + A_2 M_2^{-1} N_2 \bar{\mathbf{f}}_{l,m}^{n+1} + A_3 M_3^{-1} N_3 \bar{\mathbf{f}}_{l,m}^{n+1}] \quad (32)$$

Theorem 1: *The proposed computational scheme and compact spatial discretization converge for the vector-matrix Eq. (30).*

Proof 1: The proof of this theorem begins with the following exact scheme.

$$\bar{\mathbf{F}}_{l,m}^{n+1} = \mathbf{F}_{l,m}^n e^{-2\Delta t} + \left(\frac{-e^{-2\Delta t} + 1}{2} \right) [A_1 M_1^{-1} N_1 \mathbf{F}_{l,m}^n + A_2 M_2^{-1} N_2 \mathbf{F}_{l,m}^n + A_3 M_3^{-1} N_3 \mathbf{F}_{l,m}^n + 2\mathbf{F}_{l,m}^n] \tag{33}$$

$$\mathbf{F}_{l,m}^{n+1} = a\mathbf{F}_{l,m}^n + b\bar{\mathbf{F}}_{l,m}^{n+1} + (e^{\Delta t} - 1) [A_1 M_1^{-1} N_1 \bar{\mathbf{F}}_{l,m}^{n+1} + A_2 M_2^{-1} N_2 \bar{\mathbf{F}}_{l,m}^{n+1} + A_3 M_3^{-1} N_3 \bar{\mathbf{F}}_{l,m}^{n+1}] \tag{34}$$

After subtracting Eq. (31) from (33) and let $\mathbf{f}_{i,j}^n - \mathbf{F}_{i,j}^n = \mathbf{E}_{i,j}^n$, etc.

$$\bar{\mathbf{E}}_{l,m}^{n+1} = \mathbf{E}_{l,m}^n e^{-2\Delta t} + \left(\frac{-e^{-2\Delta t} + 1}{2} \right) [A_1 M_1^{-1} N_1 \mathbf{E}_{l,m}^n + A_2 M_2^{-1} N_2 \mathbf{E}_{l,m}^n + A_3 M_3^{-1} N_3 \mathbf{E}_{l,m}^n + 2\mathbf{E}_{l,m}^n] \tag{35}$$

Upon taking $\|\cdot\|_\infty$ on both sides of Eq. (35), it is obtained:

$$\bar{E}^{n+1} = E^n e^{-2\Delta t} + \left| \frac{-e^{-2\Delta t} + 1}{2} \right| [\|A_1 M_1^{-1} N_1\|_\infty E^n + \|A_2 M_2^{-1} N_2\|_\infty E^n + \|A_3 M_3^{-1} N_3\|_\infty E^n + E^n] \tag{36}$$

Rewrite Eq. (36) as:

$$\bar{E}^{n+1} = \lambda_1 E^n \tag{37}$$

where $\lambda_1 = e^{-2\Delta t} + \left| \frac{-e^{-2\Delta t} + 1}{2} \right| [\|A_1 M_1^{-1} N_1\|_\infty + \|A_2 M_2^{-1} N_2\|_\infty + \|A_3 M_3^{-1} N_3\|_\infty + 2]$.

Now, subtracting (32) from (34) yields.

$$\mathbf{E}_{l,m}^{n+1} = a\mathbf{E}_{l,m}^n + b\bar{\mathbf{E}}_{l,m}^{n+1} + (e^{\Delta t} - 1) [A_1 M_1^{-1} N_1 \bar{\mathbf{E}}_{l,m}^{n+1} + A_2 M_2^{-1} N_2 \bar{\mathbf{E}}_{l,m}^{n+1} + A_3 M_3^{-1} N_3 \bar{\mathbf{E}}_{l,m}^{n+1}] \tag{38}$$

By applying norm $\|\cdot\|_\infty$ on both sides of Eq. (38) is:

$$E^{n+1} = aE^n + b\bar{E}^{n+1} + c|e^{\Delta t} - 1| [\|A_1 M_1^{-1} N_1\|_\infty \bar{E}^{n+1} + \|A_2 M_2^{-1} N_2\|_\infty \bar{E}^{n+1} + \|A_3 M_3^{-1} N_3\|_\infty \bar{E}^{n+1}] \tag{39}$$

By using inequality (37) in inequality (39), the resulting inequality can be expressed as:

$$E^{n+1} \leq \lambda_2 E^n + R \left(O \left((\Delta t)^3, (\Delta x)^6, (\Delta y)^6 \right) \right) \tag{40}$$

where $\lambda_2 = a + b\lambda_1 + c|e^{\Delta t} - 1| \{A_1 M_1^{-1} N_1 + A_2 M_2^{-1} N_2 + A_3 M_3^{-1} N_3 + 1\} \delta_1$.

By using $n = 0$ in inequality (40).

$$E^1 \leq \lambda_2 E^0 + R \left(O \left((\Delta t)^3, (\Delta x)^6, (\Delta y)^6 \right) \right) \tag{41}$$

Since $E^0 = 0$, the resulting inequality (41) is:

$$E^1 \leq R \left(O \left((\Delta t)^3, (\Delta x)^6, (\Delta y)^6 \right) \right) \tag{42}$$

In inequality (40), suppose $n = 1$.

$$E^2 \leq \lambda_2 E^1 + R \left(O \left((\Delta t)^3, (\Delta x)^6, (\Delta y)^6 \right) \right) \leq (\lambda_2 + 1)R \left(O \left((\Delta t)^3, (\Delta x)^6, (\Delta y)^6 \right) \right) \tag{43}$$

If this is continued, then for a finite number of n .

$$E^n \leq (\lambda_2^{n-1} + \dots + \lambda_2 + 1) R \left(O \left((\Delta t)^3, (\Delta x)^6, (\Delta y)^6 \right) \right) = \frac{(1 - \lambda_2^n)}{1 - \lambda_2} R \left(O \left((\Delta t)^3, (\Delta x)^6, (\Delta y)^6 \right) \right) \quad (44)$$

When the infinite limits apply, then the infinite geometric series $\dots + \lambda_2^n + \dots + \lambda_2 + 1$ will converge if $|\lambda_2| < 1$. \square

4 Problem Formulations

Think about the non-Newtonian, incompressible, laminar, erratic flow across the fixed plate. The y^* -axis is perpendicular to the x^* -axis, which is taken vertically along the plate. The flow is driven by temperature and concentration gradients, causing thermal and solutal buoyancy forces. The plate surface is warmer and more concentrated than the surrounding fluid. Assume that the concentration and temperature at the plate are higher than the ambient concentration and temperature outside the plate. A transverse magnetic field of strength B_0 is applied perpendicular to the plate. It introduces a Lorentz force, which influences fluid motion through magnetohydrodynamic (MHD) effects. This is relevant in MHD flow control, cooling of microelectronics, and biofluid manipulation. The fluid obeys the Carreau model, capturing shear-thinning behaviour relevant to fluids like blood or polymeric solutions. An electric field is applied, inducing electro-osmotic motion through the electric double layer (EDL) formed near the charged surface. This mechanism is essential in lab-on-a-chip systems and micro-pumps. Porous medium effects (Darcy and Forchheimer resistance) are included, simulating real-world channels or membranes. Fig. 1 illustrates the geometry of the problem. This geometrical setup is physically relevant for BioMEMS, environmental microdevices, micro-reactors, and electrokinetic separation systems, offering a comprehensive simulation framework for complex multiphysics microflows.

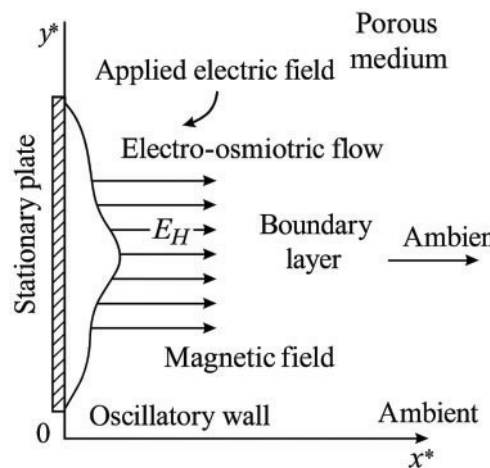


Figure 1: Geometry of the Problem

Think about the assumptions about the boundary layer; the equations that regulate the flow phenomena are expressed as [26]:

$$\frac{\partial u^*}{\partial t^*} = \underbrace{\nu \left(1 + \left(\Gamma \frac{\partial u^*}{\partial y^*} \right)^2 \right)^{\frac{m-1}{2}} \frac{\partial^2 u^*}{\partial y^{*2}}}_{\text{Non-Newtonian viscous diffusion}} + \underbrace{\nu (m-1) \Gamma^2 \frac{\partial^2 u^*}{\partial y^{*2}} \left(\frac{\partial u^*}{\partial y^*} \right)^2 \left(1 + \left(\Gamma \frac{\partial u^*}{\partial y^*} \right)^2 \right)^{\frac{n-3}{2}}}_{\text{Carreau fluid correction term}} - \underbrace{\left(\frac{\sigma B_o^2}{\rho} + \frac{\nu}{k} \right) u^*}_{\text{Magnetic+Darcy resistance}} - \underbrace{\bar{b} u^{*2}}_{\text{Forchheimer resistance}} + \underbrace{\frac{\rho_e E_x}{\rho}}_{\text{Electro-osmotic body force}} + \underbrace{g\beta_T (T - T_\infty)}_{\text{Thermal buoyancy}} + \underbrace{g\beta_c (C - C_\infty)}_{\text{Solutal buoyancy}} \quad (45)$$

$$\frac{\partial T}{\partial t^*} = \underbrace{\frac{1}{\rho c_p} \frac{\partial}{\partial y^*} \left(k(T) \frac{\partial T}{\partial y^*} \right)}_{\text{Heat conduction with variable thermal conductivity}} + \underbrace{q'''}_{\text{Volumetric heat generation}} \quad (46)$$

$$\frac{\partial C}{\partial t^*} = \underbrace{D_B \frac{\partial^2 C}{\partial y^{*2}}}_{\text{Mass diffusion}} - \underbrace{k_1 (C - C_\infty)}_{\text{First order chemical reaction}} \quad (47)$$

Momentum Eq. (45): This equation is derived from the modified Navier-Stokes equation for a Carreau fluid: $\frac{\partial u^*}{\partial t^*}$ represents the time evolution of horizontal velocity, the unsteady inertial term, the first term on the right-hand side is non-Newtonian viscous diffusion, the second term is Carreau-based non-linear viscosity, $\frac{\sigma B_o^2}{\rho}$: represents the Lorentz force due to the applied magnetic field, $\frac{\nu}{k}$ is flow resistance through porous medium (Darcy term), $\bar{b} u^{*2}$ represents Inertial resistance Forchheimer’s term for non-linear drag, $\rho_e E_x$: showing the electric body force inducing electro-osmotic motion, $g\beta_T (T - T_\infty)$: represents buoyancy from temperature gradient and $g\beta_c (C - C_\infty)$: represents the buoyancy from the concentration gradient.

Energy (Temperature) Eq. (46): $\frac{\partial T}{\partial t^*}$: represents the time-dependent temperature change, $k(T) = k_\infty \left(1 + \varepsilon_1 \frac{T - T_\infty}{T_w - T_\infty} \right)$ is variable thermal conductivity and $q''' = \frac{k u_R}{\rho x^* \nu c_p} (A^* u (T_w - T_\infty) + B^* (T - T_\infty))$ represents the internal heat generation due to joule heating (electrokinetic effect) and viscous dissipation or other sources.

Concentration Eq. (47): $\frac{\partial C}{\partial t^*}$: represents the time-dependent change in species concentration, D_B is mass diffusivity (Brownian diffusion coefficient), $\frac{\partial^2 C}{\partial y^{*2}}$: represents the diffusive transport in the vertical direction and $k_1 (C - C_\infty)$ is the rate of chemical reaction depleting species, assumed first-order (e.g., absorption or degradation). Subject to initial and boundary conditions.

$$\left. \begin{aligned} &u^* = 0, T = T_\infty, C = C_\infty \text{ when } t^* = 0 \\ &u^* = 0, T = T_\infty + \varepsilon_1 (T_w - T_\infty) \cos w^* t^*, C = C_\infty + \varepsilon_1 (C - C_\infty) \cos w^* t^* \text{ when } y^* = 0 \\ &u \rightarrow 0, T \rightarrow T_\infty, C \rightarrow C_\infty \text{ when } y^* \rightarrow \infty \end{aligned} \right\} \quad (48)$$

at initial state $t = 0$ fluid is at rest and ambient conditions. At the plate $y^* = 0$, the wall velocity is zero, whereas temperature and concentration oscillate harmonically. When far away from the plate $y^* \rightarrow \infty$ the fluid properties approach ambient values. This setup simulates time-varying wall conditions in biological tissues or surface-treated membranes exposed to periodic thermal or concentration cycles. The velocity boundary condition at the wall is set to reflect no-slip or oscillatory slip induced by electro-osmotic effects, which is consistent with charged microchannel surfaces exposed to external electric fields. The imposed time-dependent slip velocity mimics scenarios such as alternating-current electro-osmosis (ACEO) or pulsatile pumping mechanisms in lab-on-a-chip devices. The thermal boundary condition assumes a temperature at

the wall higher than the ambient temperature, often encountered in thermally regulated microfluidic devices, thermal cycling chambers (e.g., for PCR applications), or localized Joule heating in electrokinetic setups. Where u^* and v^* are a horizontal and vertical component of velocity, respectively, T is the temperature of the fluid, C is concentration, respectively, β_T is the coefficient of thermal convection, β_c is the coefficient of solutal convection, g is gravity, Γ is a material, fluid parameter, ν denotes kinematic viscosity, σ is electrical conductivity, \bar{b} is non-Darcian parameter, k_1 is reaction rate parameter, k denotes permeability constant, E_x is electric field component, ρ is the density of the fluid, ρ_e is the total ionic density. Let B_o is the strength of the magnetic field applied transversely to the plate, c_p is the specific heat capacity, k_∞ represents liquid thermal conductivity and ε_1 represents smaller parameters elaborating temperature characteristics for thermal-dependent conductivity.

Consider the following transformations [26] to convert (45)–(49) into dimensionless partial differential equations.

$$y = \frac{y^*}{L_R}, u = \frac{u^*}{u_R}, v_o = \frac{v_1}{u_R}, w = t_R w^*, t = \frac{t^*}{t_R}, \phi = \frac{\phi^*}{\zeta}, \theta = \frac{T - T_\infty}{T_w - T_\infty}, \phi = \frac{C - C_\infty}{C_w - C_\infty} \quad (49)$$

where $u_R = (\nu g \beta_T \Delta T)^{1/3}$, $L_R = \left(\frac{g \beta_T \Delta T}{\nu^2}\right)^{-1/3}$ and $t_R = (g \beta_T \Delta T)^{-2/3} \nu^{1/3}$. These non-dimensionalizations simplify the equations and reveal governing parameters like Weissenberg number, magnetic parameter, Darcy number, etc.

Derive Dimensionless Governing Eqs. (50)–(52): Eqs. (45)–(47) can be rewritten as dimensionless governing equations by using transformations (49).

$$\begin{aligned} \frac{\partial u}{\partial t} = & \underbrace{\left(1 + W_e^2 \left(\frac{\partial u}{\partial y}\right)^2\right)^{\frac{n-1}{2}} \frac{\partial^2 u}{\partial y^2}}_{\text{Shear dependent viscosity (Carreay term)}} + \underbrace{(m-1) W_e^2 \frac{\partial^2 u}{\partial y^2} \left(\frac{\partial u}{\partial y}\right)^2 \left(1 + W_e^2 \left(\frac{\partial u}{\partial y}\right)^2\right)^{\frac{n-3}{2}}}_{\text{non-Newtonian correction}} \\ & - \underbrace{\left(M + \frac{1}{D_a}\right) u}_{\text{Magnetic + Darcy porous drag}} - \underbrace{F_s u^2}_{\text{Forchheimer resistance}} + \underbrace{U_{HS} m_e^2 e^{-m_e y}}_{\text{Electro-osmotic velocity}} \\ & + \underbrace{\theta}_{\text{Thermal buoyancy}} + \underbrace{NC}_{\text{Solutal buoyancy}} \end{aligned} \quad (50)$$

$$\frac{\partial \theta}{\partial t} = \underbrace{\frac{1}{P_r} (1 + \varepsilon_2 \theta) \frac{\partial^2 \theta}{\partial y^2}}_{\text{Heat conduction with variable}} + \underbrace{\frac{\varepsilon_2}{P_r} \left(\frac{\partial \theta}{\partial y}\right)^2}_{\text{Nonlinear conduction (temperature sensitivity)}} + \underbrace{\frac{\varepsilon}{P_r} (A^* u + B^* \theta)}_{\text{Internal heat generation}} \quad (51)$$

$$\frac{\partial \phi}{\partial t} = \underbrace{\frac{1}{S_c R_e} \frac{\partial^2 \phi}{\partial y^2}}_{\text{Mass diffusion}} - \underbrace{\gamma \phi}_{\text{First order chemical reaction}} \quad (52)$$

subject to the dimensionless initial and boundary conditions.

$$\left. \begin{aligned} u = 0, \theta = 0, \phi = 0 \text{ for } t = 0 \\ u = 0, \theta = \varepsilon_1 \cos w^* t, \phi = \varepsilon_1 \cos w^* t \text{ for } y = 0 \\ u \rightarrow 0, \theta \rightarrow 0, \phi \rightarrow 0 \text{ for } y \rightarrow \infty \end{aligned} \right\} \quad (53)$$

where D_a is Darcy's number, W_e is a Weissenberg number, N represents the Buoyancy ratio, M is the magnetic parameter, P_r is the Prandtl number, S_c is Schmidt number, ε and ε_1 are dimensionless parameters, F_s represents Forchheimer number, k_c dimensionless reaction rate parameter, $U_{HS} m_e^2 e^{-m_e y}$: represents electro-osmotic body force due to EDL potential, and these are defined as:

$$D_a = \frac{k}{\nu t_R}, W_e = \frac{\Gamma u_R}{L_R}, N = \frac{\beta_c (C_w - C_\infty)}{\beta_T (T_w - T_\infty)}, M = \frac{t_R \sigma B_o^2}{\rho}, P_r = \frac{\nu k}{\rho c_p}, S_c = \frac{\nu}{D}, \varepsilon = \frac{t_R u_R}{x^*}, F_s = \bar{b} u_R t_R, k_c = t_R k_1$$

These terms together model realistic non-linear thermal behaviour, such as temperature-dependent conduction and Joule heating in electrokinetic applications, and also capture species diffusion and chemical consumption or generation, such as nutrient uptake, pollutant decay, or reaction in catalytic membranes.

To quantify mass transfer at the wall: The local Sherwood number measures the rate of species diffusion and is defined as:

$$S_h = \frac{L q_j}{D_B (C_w - C_\infty)} \quad (54)$$

where $q_j = -D_B \left. \frac{\partial C}{\partial y^*} \right|_{y^*=0}$.

By using transformations (50), the dimensionless local Sherwood number is given as:

$$S_{hL} = - \left. \frac{\partial \phi}{\partial y} \right|_{y=0} \quad (55)$$

This is crucial in engineering processes like filtration, separation, and biochemical transport.

Real-World Applications: The suggested model is pertinent to practical uses where non-Newtonian fluid behaviour and electro-osmotic transport are vital. In biomedical engineering, where the Carreau model precisely reflects the shear-thinning character of real fluids, it can represent blood flow in microfluidic devices or tissue scaffolds. The model is appropriate for diagnostic lab-on-a-chip platforms and medication delivery systems, including heat and mass transfer with variable thermal conductivity, since thermal management and species diffusion are critical. Furthermore, combining electric fields and porous media influences fits sophisticated membrane filtration, electrokinetic desalination, and wastewater treatment technologies. Magnetic field interaction increases its relevance to magnetohydrodynamic pumps and bioMEMS, where external magnetic control governs flow. The model is flexible for maximizing fluid movement in micro/nano-scale engineering systems spanning environmental, energy, and healthcare sectors.

5 Results and Discussion

We conduct an extensive simulation study with the following aims:

1. We demonstrate the application of the proposed two-stage explicit scheme for solving non-linear time-dependent differential equations, as introduced in [Section 4](#).
2. We highlight the efficiency of the predictor stage in estimating the solution at the $(n + 1)$ th time level using only the known values at the n th time level without requiring iterative procedures.
3. We showcase the corrector stage's role in refining the predictor values, thereby enhancing temporal accuracy and ensuring the stability of the numerical results.
4. We emphasize the advantages of the explicit scheme, particularly its ability to handle non-linear terms without the need for linearization or additional solvers.

- We validate that the proposed scheme effectively captures the dynamics of electro-osmotic flow in Carreau fluids, even in the presence of magnetic fields, porous medium effects, and non-linear thermal and solutal transport mechanisms.

5.1 Velocity Profile Analysis

Effect of the Weissenberg Number W_e on Velocity Profile: Fig. 2 illustrates the impact of the Weissenberg number W_e on the velocity profile for the electro-osmotic flow of Carreau fluid over a stationary plate. The simulation is performed using the parameter set: $m = 1.5$, $Da = 7$, $m_e = 0.5$, $Pr = 0.9$, $Sc = 0.9$, $\gamma = 0.1$, $\varepsilon_1 = 0.7$, $\varepsilon = 0.1$, $\varepsilon_2 = 0.1$, $Fs = 0.1$, $U_{HS} = 0.1$, $N = 0.1$, $M = 0.1$, $A^* = 0.1$, $B^* = 0.1$. The velocity profiles are plotted for three different values of the Weissenberg number: $W_e = 0.1$, $W_e = 5.0$ and $W_e = 9.0$. As W_e the velocity profile exhibits a significant decline in magnitude, particularly near the boundary layer region. The reduction in peak velocity with increasing W_e reflects the enhanced elastic nature of the fluid, which resists deformation and slows down the momentum transport. This is a characteristic feature of non-Newtonian viscoelastic fluids, such as polymer solutions or biological fluids, where the fluid's relaxation time becomes comparable to the timescale of flow.

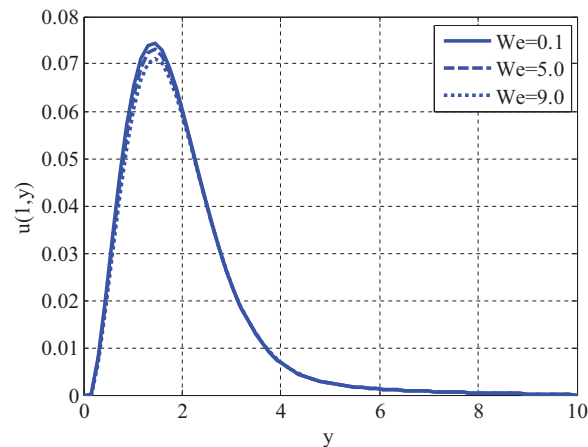


Figure 2: Variation of Weissenberg number on velocity profile using $m = 1.5$, $Da = 7$, $m_e = 0.5$, $Pr = 0.9$, $Sc = 0.9$, $\gamma = 0.1$, $\varepsilon_1 = 0.7$, $\varepsilon = 0.1$, $\varepsilon_2 = 0.1$, $Fs = 0.1$, $U_{HS} = 0.1$, $N = 0.1$, $M = 0.1$, $A^* = 0.1$, $B^* = 0.1$

Effect of Magnetic Parameter M on Velocity Profile: Fig. 3 presents the influence of the magnetic parameter M on the velocity profile of electro-osmotic flow in a Carreau fluid. The simulation is carried out under the fixed parameter values: $m = 1.5$, $Da = 7$, $m_e = 0.5$, $Pr = 0.9$, $Sc = 0.9$, $\gamma = 0.1$, $\varepsilon_1 = 0.7$, $\varepsilon = 0.1$, $\varepsilon_2 = 0.1$, $Fs = 0.1$, $U_{HS} = 0.1$, $N = 0.1$, $We = 0.1$, $A^* = 0.1$, $B^* = 0.1$. The velocity profiles are plotted for three values of the magnetic parameter: $M = 0.1$, $M = 5.0$, and $M = 9.0$. As shown in the figure, the velocity profile decreases consistently with increasing M . The Lorentz force, which is a resistive force when a transverse magnetic field is present, is responsible for this slowing down. As M increases, the magnitude of the Lorentz force also increases, thereby enhancing flow resistance and suppressing the motion of the electrically conducting fluid. The magnetic parameter M represents the ratio of electromagnetic force to viscous force. In an electrically conducting fluid, the interaction between the applied magnetic field and the electric current generated by electro-osmotic motion induces a Lorentz force, which opposes the fluid flow. This magnetohydrodynamic (MHD) braking effect becomes more pronounced at higher M , leading to a flatter and less intense velocity profile.

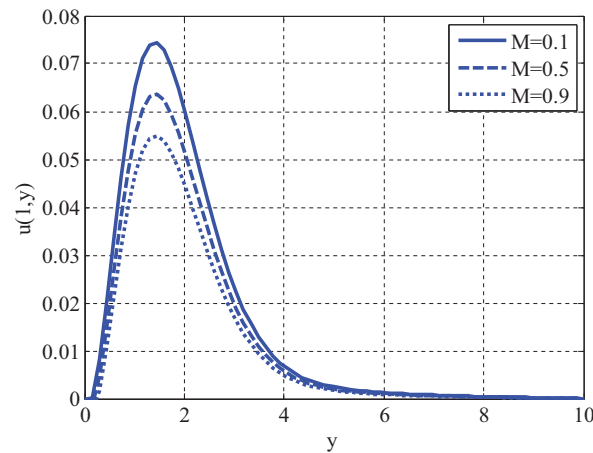


Figure 3: Variation of magnetic parameter on velocity profile using $m = 1.5, Da = 7, m_e = 0.5, Pr = 0.9, Sc = 0.9, \gamma = 0.1, \epsilon_1 = 0.7, \epsilon = 0.1, \epsilon_2 = 0.1, Fs = 0.1, U_{HS} = 0.1, N = 0.1, We = 0.1, A^* = 0.1, B^* = 0.1$

Effect of Helmholtz–Smoluchowski Velocity U_{HS} on Velocity Profile: [Fig. 4](#) illustrates the influence of the Helmholtz–Smoluchowski velocity U_{HS} on the velocity profile of electro-osmotic flow in a Carreau fluid. The simulation is carried out under the parameter values: $m = 1.5, Da = 7, m_e = 0.5, Pr = 0.9, Sc = 0.9, \gamma = 0.1, \epsilon_1 = 0.7, \epsilon = 0.1, \epsilon_2 = 0.1, Fs = 0.1, M = 0.1, N = 0.1, We = 0.1, A^* = 0.1, B^* = 0.1$. The velocity profiles are plotted for three values of $U_{HS} = 0.1, U_{HS} = 0.25$ and $U_{HS} = 0.5$. It is observed that as U_{HS} increases, the peak velocity of the flow profile increases significantly, and the flow becomes steeper near the wall. This enhancement in velocity is a direct consequence of the stronger electro-osmotic force induced at the fluid–solid interface. The Helmholtz–Smoluchowski velocity U_{HS} represents the slip velocity generated at the wall due to electrokinetic effects. A higher U_{HS} corresponds to a stronger electrostatic interaction between the electric field and the charged double layer at the boundary. This produces greater Coulomb forces, which drive the fluid more effectively, resulting in faster and more intense electro-osmotic transport.

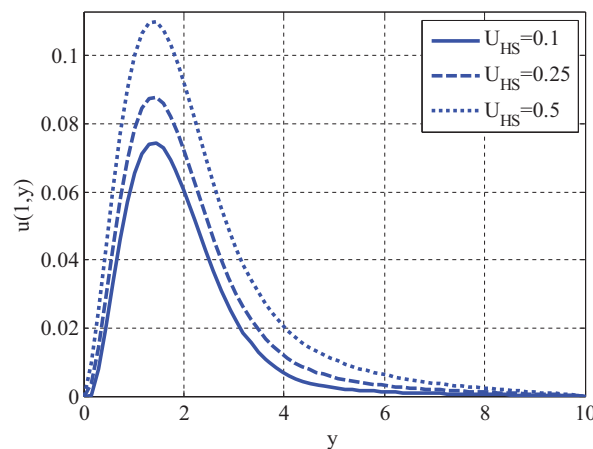


Figure 4: Variation of Helmholtz Smoluchowski velocity on velocity profile using $m = 1.5, Da = 7, m_e = 0.5, Pr = 0.9, Sc = 0.9, \gamma = 0.1, \epsilon_1 = 0.7, \epsilon = 0.1, \epsilon_2 = 0.1, Fs = 0.1, M = 0.1, N = 0.1, We = 0.1, A^* = 0.1, B^* = 0.1$

Effect of Electro-Osmotic Parameter m_e on Velocity Profile: Fig. 5 demonstrates the effect of the electro-osmotic parameter m_e on the velocity profile of a Carreau fluid under electro-osmotic flow. The simulation is conducted using the parameter set: $m = 1.5$, $Da = 7$, $U_{HS} = 0.1$, $Pr = 0.9$, $Sc = 0.9$, $\gamma = 0.1$, $\varepsilon_1 = 0.7$, $\varepsilon = 0.1$, $\varepsilon_2 = 0.1$, $Fs = 0.1$, $M = 0.1$, $N = 0.1$, $We = 0.1$, $A^* = 0.1$, $B^* = 0.1$. The velocity profiles are displayed for three different values of $m_e = 0.5, 0.9, 1.4$. The figure shows that as m_e increases, the peak velocity also increases, indicating an overall enhancement of the electro-osmotic flow. The flow acceleration is more significant near the wall and diminishes further into the fluid domain. The parameter m_e characterizes the penetration depth of the electric double layer (EDL) and reflects the influence of the applied electric field on the flow. An increase in m_e strengthens the interaction between the wall's surface charge and the electrolyte, resulting in a stronger Coulomb force acting on the fluid. This electrokinetic effect accelerates the flow, particularly near the boundary where the EDL is most prominent. Higher values of m_e correspond to greater electric field influence over a wider fluid region, leading to increased momentum generation and higher velocity throughout the near-wall region. However, this effect gradually levels off away from the wall due to decay in the electric potential.

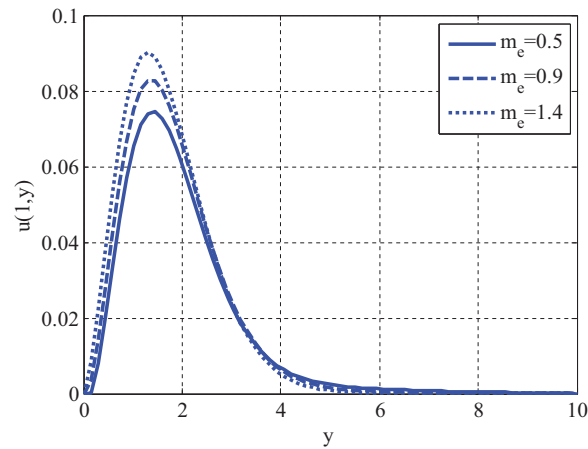


Figure 5: Variation of electro-osmotic parameter on velocity profile using $m = 1.5$, $Da = 7$, $U_{HS} = 0.1$, $Pr = 0.9$, $Sc = 0.9$, $\gamma = 0.1$, $\varepsilon_1 = 0.7$, $\varepsilon = 0.1$, $\varepsilon_2 = 0.1$, $Fs = 0.1$, $M = 0.1$, $N = 0.1$, $We = 0.1$, $A^* = 0.1$, $B^* = 0.1$

5.2 Temperature Profile Analysis

Effect of Prandtl Number P_r on Temperature Profile: Fig. 6 illustrates the effect of the Prandtl number P_r on the temperature distribution within the flow domain for a Carreau fluid under electro-osmotic influence. The simulation is performed using the following parameter values: $m = 1.5$, $Da = 7$, $U_{HS} = 0.1$, $m_e = 0.5$, $Sc = 0.9$, $\gamma = 0.1$, $\varepsilon_1 = 0.7$, $\varepsilon = 0.1$, $\varepsilon_2 = 0.1$, $Fs = 0.1$, $M = 0.1$, $N = 0.1$, $We = 0.1$, $A^* = 0.1$, $B^* = 0.1$. The temperature profiles are shown for three different values of the Prandtl number: $P_r = 0.9$, $P_r = 1.3$ and $P_r = 1.7$. The results show that increasing the Prandtl number causes a slight decrease in the temperature profile, especially beyond the thermal boundary layer region. This trend reflects the inverse relationship between P_r and thermal diffusivity. The Prandtl number P_r represents the ratio of momentum diffusivity (viscous diffusion) to thermal diffusivity. A higher P_r value indicates that thermal diffusion is slower than momentum diffusion, leading to thinner thermal boundary layers and, thus, lower temperature penetration into the fluid domain. At lower P_r , thermal conductivity is relatively higher, allowing heat to diffuse more efficiently through the fluid. As P_r increases, this conductivity weakens, reducing the heat transfer capability and resulting in a flatter, less intense temperature profile.

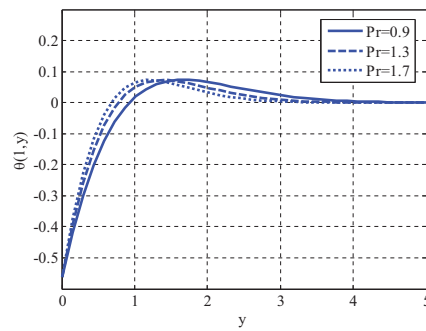


Figure 6: Variation of Prandtl number on temperature profile using $m = 1.5, Da = 7, U_{HS} = 0.1, m_e = 0.5, Sc = 0.9, \gamma = 0.1, \epsilon_1 = 0.7, \epsilon = 0.1, \epsilon_2 = 0.1, Fs = 0.1, M = 0.1, N = 0.1, We = 0.1, A^* = 0.1, B^* = 0.1$

Effect of the Small Parameter ϵ_2 in Variable Thermal Conductivity on Temperature Profile: [Fig. 7](#) illustrates the influence of the small parameter ϵ_2 , embedded within the model for variable thermal conductivity on the temperature distribution in the electro-osmotic flow of Carreau fluid. The simulation is conducted using the parameters: $m = 1.5, Da = 7, U_{HS} = 0.1, m_e = 0.5, Sc = 0.9, \gamma = 0.1, \epsilon_1 = 0.7, \epsilon = 0.1, Pr = 0.9, Fs = 0.1, M = 0.1, N = 0.1, We = 0.1, A^* = 0.1, B^* = 0.1$. The figure presents temperature profiles for three values of $\epsilon_2 = 0.1, 0.5, 0.9$. As seen in the figure, the temperature profile increases with increasing ϵ_2 . The peak temperature rises gradually, indicating that a larger value of ϵ_2 enhances the thermal conductivity of the fluid, thereby improving heat transfer within the system. The parameter ϵ_2 governs how strongly thermal conductivity varies with temperature. A higher value of ϵ_2 implies that conductivity becomes more sensitive to temperature changes, increasing more significantly in regions of elevated temperature. As a result, more heat is conducted away from the hot boundary, and the fluid domain experiences enhanced thermal diffusion, leading to broader and higher temperature profiles. This improved conductivity results in a thicker thermal boundary layer and more efficient energy distribution throughout the fluid.

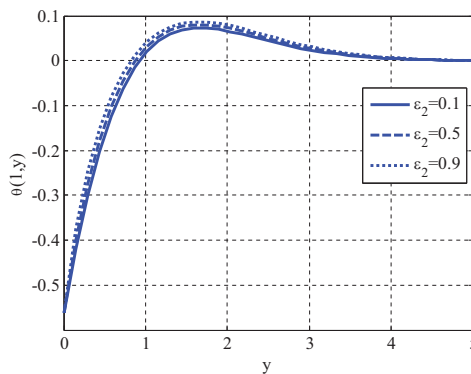


Figure 7: Variation of small parameter contained in variable thermal conductivity on temperature profile using $m = 1.5, Da = 7, U_{HS} = 0.1, m_e = 0.5, Sc = 0.9, \gamma = 0.1, \epsilon_1 = 0.7, \epsilon = 0.1, Pr = 0.9, Fs = 0.1, M = 0.1, N = 0.1, We = 0.1, A^* = 0.1, B^* = 0.1$

5.3 Concentration Profile Analysis

Effect of Reaction Rate Parameter γ on Concentration Profile: [Fig. 8](#) presents the influence of the reaction rate parameter γ on the concentration distribution in an electro-osmotically driven flow of Carreau fluid. The simulation is conducted using the parameter values: $m = 1.5, Da = 7, U_{HS} = 0.1, m_e = 0.5, Sc = 0.9,$

$\varepsilon_2 = 0.1, \varepsilon_1 = 0.7, \varepsilon = 0.1, Pr = 0.9, Fs = 0.1, M = 0.1, N = 0.1, We = 0.1, A^* = 0.1, B^* = 0.1$. The concentration profiles are displayed for three different values of the reaction rate parameter: $\gamma = 0.1, 0.5, 0.9$. As evident from the figure, an increase in γ leads to a decrease in the concentration profile. The peak concentration decreases progressively with higher γ , indicating the enhanced concentration depletion due to stronger chemical reactions. The parameter γ represents the rate at which a solute undergoes a first-order chemical reaction, consuming the concentration species as it proceeds. A higher γ indicates a faster conversion of the solute into a product, thereby reducing the concentration of the species throughout the flow domain. This behaviour is more pronounced near the wall, where the concentration gradient is steepest and the chemical activity is most dominant. As γ increases, concentration diffusion is outpaced by its consumption, leading to a thinner concentration boundary layer and lower concentration levels overall.

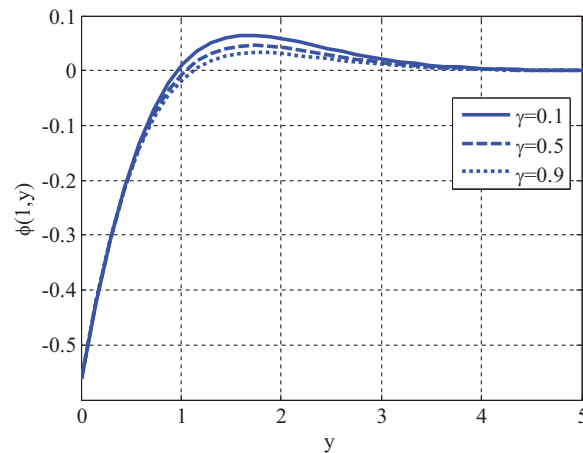


Figure 8: Variation of reaction rate parameter on concentration profile using $m = 1.5, Da = 7, U_{HS} = 0.1, m_e = 0.5, Sc = 0.9, \varepsilon_2 = 0.1, \varepsilon_1 = 0.7, \varepsilon = 0.1, Pr = 0.9, Fs = 0.1, M = 0.1, N = 0.1, We = 0.1, A^* = 0.1, B^* = 0.1$

5.4 Sherwood Number Analysis

Effect of Schmidt Number and Reaction Rate Parameter γ on Local Sherwood Number: [Fig. 9](#) displays the variation of the local Sherwood number as a function of the Schmidt number Sc for three different values of the reaction rate parameter $\gamma = 0.1, 0.4, 0.7$. The simulation is performed using the following parameters: $m = 1.5, Da = 7, U_{HS} = 0.1, m_e = 0.5, \varepsilon_2 = 0.1, \varepsilon_1 = 0.7, \varepsilon = 0.1, Pr = 0.9, Fs = 0.1, M = 0.1, N = 0.1, We = 0.1, A^* = 0.1, B^* = 0.1$. As shown in the figure, the local Sherwood number decreases with increasing Sc , and this decreasing trend is further intensified for higher values of γ . This implies that mass transfer at the wall reduces as molecular diffusivity decreases and reaction rates increase. The Schmidt number $Sc = \frac{\nu}{D}$ is the ratio of momentum diffusivity to mass diffusivity. A higher Sc corresponds to lower mass diffusion, which hinders species transport toward the wall and thereby reduces the Sherwood number, a measure of mass transfer rate. The reaction rate parameter γ controls the rate at which the solute is consumed. A higher γ leads to a more rapid depletion of the species near the boundary, lowering the concentration gradient and, thus, the Sherwood number. The combination of these parameters demonstrates that weaker diffusion and stronger reaction kinetics diminish mass flux, as measured by the Sherwood number.

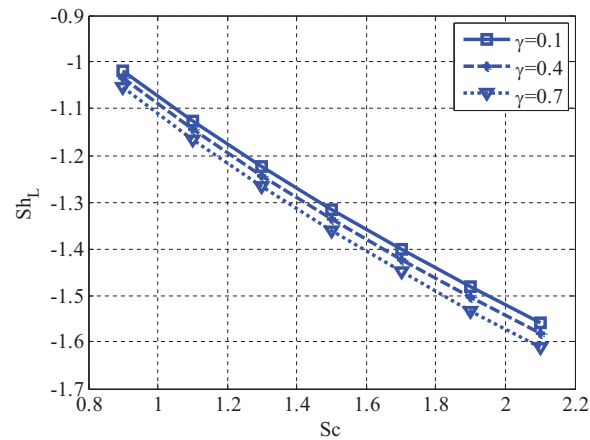


Figure 9: Variation of Schmidt number and reaction rate parameter on local Sherwood number using $m = 1.5$, $Da = 7$, $U_{HS} = 0.1$, $m_e = 0.5$, $\epsilon_2 = 0.1$, $\epsilon_1 = 0.7$, $\epsilon = 0.1$, $Pr = 0.9$, $F_s = 0.1$, $M = 0.1$, $N = 0.1$, $We = 0.1$, $A^* = 0.1$, $B^* = 0.1$

5.5 3D Mesh and Contour Plot Analysis

Contour Plot for the Horizontal Velocity Component: [Fig. 10](#) presents the contour plot of the horizontal velocity component in an electro-osmotic flow of Carreau fluid over a stationary plate. The simulation uses the parameter values: $m = 1.5$, $Da = 7$, $U_{HS} = 0.1$, $m_e = 0.5$, $Sc = 0.9$, $\epsilon_2 = 0.1$, $\epsilon_1 = 0.7$, $\epsilon = 0.1$, $Pr = 0.9$, $F_s = 0.1$, $M = 0.1$, $N = 0.1$, $We = 0.1$, $A^* = 0.1$, $B^* = 0.1$, $Sc = 0.9$, $\gamma = 0.9$. The contour plot reveals a repetitive pattern of vortex-like structures along the horizontal direction, alternating positive and negative regions. This represents oscillatory behaviour in the horizontal velocity field, likely due to the time-periodic boundary conditions and the electrokinetic coupling effects. The alternating peaks and troughs in the velocity contours indicate unsteady electro-osmotic flow behaviour with localized accelerations and decelerations. These may arise from the influence of oscillatory thermal and concentration boundary inputs, leading to a periodic driving force along the plate. The non-linear interactions between the electric double layer, magnetic damping via M , and porous media resistance via Da , F_s . The closed and elongated contour loops suggest the presence of velocity cells or recirculation zones, especially near the boundary, where the electrokinetic effects are strongest. Such velocity distributions are important in practical systems like micro-mixers, where induced oscillatory flow enhances mixing performance without mechanical agitation.

Contour Plot for Temperature Distribution: [Fig. 11](#) displays the temperature contour plot for the electro-osmotic flow of a Carreau fluid under the influence of various coupled physical effects. The simulation is performed using the parameter set: $m = 1.5$, $Da = 7$, $U_{HS} = 0.1$, $m_e = 0.5$, $Sc = 0.9$, $\epsilon_2 = 0.1$, $\epsilon_1 = 0.7$, $\epsilon = 0.1$, $Pr = 0.9$, $F_s = 0.1$, $M = 0.1$, $N = 0.1$, $We = 0.1$, $A^* = 0.1$, $B^* = 0.1$, $Sc = 0.9$, $\gamma = 0.9$. The temperature contours indicate a periodic and stratified distribution of thermal zones along the horizontal direction, with intense thermal gradients close to the boundary wall. The colour-coded isotherms (lines of constant temperature) form wave-like structures, showing oscillatory thermal behaviour near the surface that gradually diminishes into the bulk fluid. This oscillatory structure in the temperature field is primarily due to internal heat generation terms involving A^*u and $B^*\theta$, which dynamically interacts with the flow velocity and temperature field to amplify localized heating near the wall. The influence of variable thermal conductivity, controlled by ϵ_2 , enhancing heat conduction in higher temperature zones. The stratification shows that thermal waves penetrate the fluid in a damped pattern, with energy dissipation over distance due to conduction and convection. Hence, [Fig. 10](#) offers deep insights into thermal transport dynamics

in electrokinetically driven non-Newtonian flows, which is crucial for designing and optimizing energy-sensitive microfluidic systems.

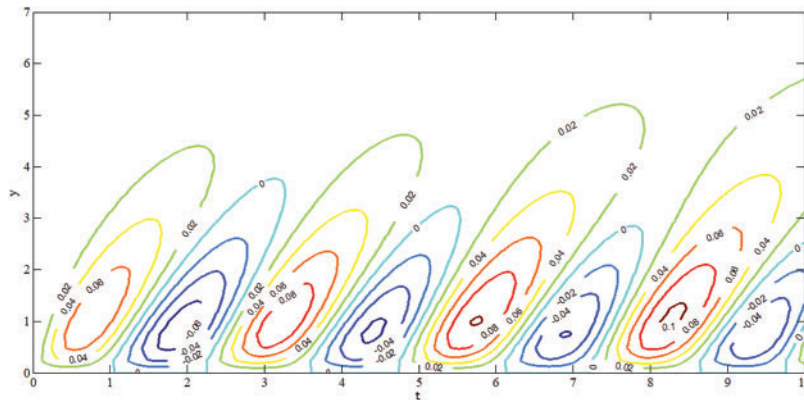


Figure 10: Contour plot for the horizontal component of velocity profile using $m = 1.5, Da = 7, U_{HS} = 0.1, m_e = 0.5, Sc = 0.9, \varepsilon_2 = 0.1, \varepsilon_1 = 0.7, \varepsilon = 0.1, Pr = 0.9, Fs = 0.1, M = 0.1, N = 0.1, We = 0.1, A^* = 0.1, B^* = 0.1, Sc = 0.9, \gamma = 0.9$

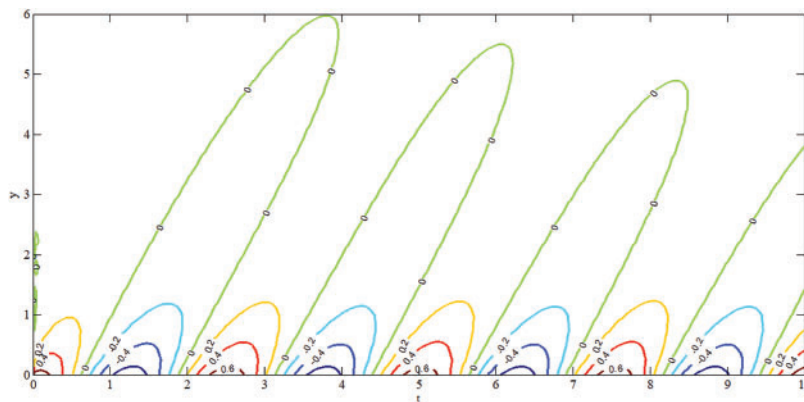


Figure 11: Contour plot for temperature profile using $m = 1.5, Da = 7, U_{HS} = 0.1, m_e = 0.5, Sc = 0.9, \varepsilon_2 = 0.1, \varepsilon_1 = 0.7, \varepsilon = 0.1, Pr = 0.9, Fs = 0.1, M = 0.1, N = 0.1, We = 0.1, A^* = 0.1, B^* = 0.1, Sc = 0.9, \gamma = 0.9$

3D Mesh Plot with Contours of Concentration Distribution: Fig. 12 presents a 3D mesh plot underneath with contour projections depicting the spatio-temporal evolution of concentration $u(t, y)$ in a reactive electro-osmotic flow of a non-Newtonian fluid. The simulation is performed with the following parameters: $Re = 1.9, m = 0.1, Ec = 0.9, H_o = 0.1, We = 0.1, Pr = 0.9, Gr_T = 1.5, \varepsilon_1 = 1, E_1 = 0.01, Sc = 0.9, \gamma = 0.1, b$ (chosen scheme) $= 1, u_w = \cos(t) \sin(t), x_L$ (length of boundary) $= 27 = y_L, t_f$ (final time) $= 10$. The parameter b represents the scheme selection value used in numerical implementation, here set as 1. The plot shows clearly defined wave-like structures that fluctuate periodically in time and decay in magnitude along the spatial direction y . The colour gradient from red to blue indicates high-to-low concentration regions, while the oscillatory patterns signify the dynamic influence of the time-periodic wall velocity condition $u_w = \cos(t) \sin(t)$. This figure captures how the concentration evolves over time and space, with the following key features: Time-dependent boundary oscillation through u_w initiates periodic pulses in concentration at the wall, which then propagate into the fluid domain. The observed amplitude decay in the y -direction reflects diffusive damping, consistent with the role of

the Schmidt number S_c and the finite reaction rate γ . The symmetrical oscillations align with sinusoidal boundary forcing and confirm the scheme's ability to accurately capture temporal and spatial phase shifts in concentration dynamics. By visualizing the time and space evolution in a single plot, Fig. 11 provides powerful insight into the interplay between convection, diffusion, and reaction kinetics in microfluidic or porous environments.

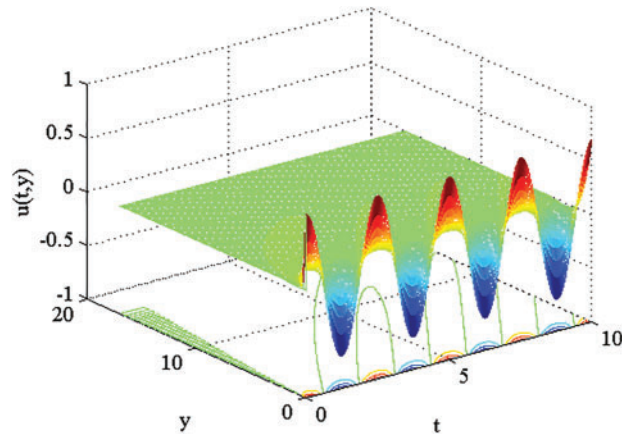


Figure 12: Mesh plot underneath contours for concentration profile using $Re = 1.9$, $m = 0.1$, $Ec = 0.9$, $H_o = 0.1$, $We = 0.1$, $Pr = 0.9$, $Gr_T = 1.5$, $\varepsilon_1 = 1$, $E_1 = 0.01$, $Sc = 0.9$, $\gamma = 0.1$, b (chosen scheme) = 1, $u_w = \cos(t) \sin(t)$, x_L (length of boundary) = 27 = y_L , t_f (final time) = 10

5.6 Selection of Physical Parameters and Their Ranges

This study's selection of physical parameters is based on values commonly reported in experimental and computational research on electro-osmotic flow, non-Newtonian Carreau fluids, and microfluidic transport phenomena. The Weissenberg number W_e is varied in the range $0.1 \leq W_e \leq 9.0$ to represent fluids with low to high elastic behaviour, relevant in polymeric and biological fluid applications. The Forchheimer number F_s is chosen between 0.1 and 1.0 to capture inertial resistance in porous media. The Darcy number D_a ranges from 10^{-2} to 10, covering both low- and high-permeability porous structures often encountered in microchannel designs. The magnetic parameter M is considered within $0.1 \leq M \leq 1.0$, consistent with low-to-moderate strength magnetic fields used in magnetohydrodynamic (MHD) control applications. Thermal and mass diffusion are modelled using Prandtl numbers $Pr \in [0.7, 2.0]$ and Schmidt numbers $S_c \in [0.6, 1.5]$, which align with values for water, biological fluids, and electrolytic solutions. The reaction rate parameter γ is explored in the range $0.1 \leq \gamma \leq 0.9$, representing weak to strong chemical reaction intensities. These parameter ranges ensure the physical realism of the simulations while maintaining numerical stability and practical relevance to BioMEMS, electrokinetic devices, and thermally sensitive microfluidic systems.

5.7 Improved Temporal Accuracy via Modified Exponential Integrator Scheme

To enhance the temporal accuracy of the initially proposed scheme for solving time-dependent partial differential equations, we introduce a modified version that surpasses the accuracy of the conventional second-order Runge-Kutta method. While the original two-stage explicit scheme provides a robust solution framework, it is not inherently more accurate than standard second-order methods for certain step sizes. Therefore, a refined formulation is developed to achieve improved precision with comparable computational effort.

The first stage of the enhanced scheme is constructed using an exponential integrator approach, followed by a slightly modified second stage, as given below:

$$\bar{p}_{l,m}^{n+1} = p_{l,m}^n e^{7.5\Delta t} + \frac{(e^{7.5\Delta t} - 1)}{7.5} \left\{ \left. \frac{\partial p}{\partial t} \right|_{l,m}^n - 7.5 p_{l,m}^n \right\} \quad (56)$$

$$p_{l,m}^{n+1} = a p_{l,m}^n + b \bar{p}_{l,m}^n + c \Delta t \left. \frac{\partial \bar{p}}{\partial t} \right|_{l,m}^{n+1} \quad (57)$$

This modified scheme is benchmarked against the existing method used in [27] through a comparative simulation of the second example problem provided therein. In this context, the diffusion term in the proposed scheme is discretized using a high-order compact difference method. In contrast, the diffusion term in the existing scheme and the convective term in both methods is discretized using second-order central difference formulas. The numerical results, summarized in Table 1, demonstrate that the improved scheme consistently yields lower numerical error than the standard Runge-Kutta scheme for the selected step sizes. This confirms its suitability for high-fidelity simulations where enhanced temporal accuracy is essential.

Table 1: Comparison of the proposed scheme with the existing Runge-Kutta Scheme for solving the convection-diffusion problem using N (grid points) = 50, t_f (final time) = 0.1

Δt	L_2 Error	
	Runge-Kutta	Proposed (New)
0.1/1000	2.6728×10^{-5}	9.3274×10^{-6}
0.1/1500	2.6724×10^{-5}	8.5933×10^{-6}
0.1/2000	2.6722×10^{-5}	1.0052×10^{-5}
0.1/2500	2.6722×10^{-5}	1.1320×10^{-5}
0.1/3000	2.6721×10^{-5}	1.2277×10^{-5}

6 Conclusions

This paper presents a modified two-stage computational strategy combining an exponential integrator with a Runge-Kutta-type algorithm created and implemented to simulate the electro-osmotic flow of Carreau fluid over a stationary plate, including the effects of heat and mass transfer. The suggested approach preserves second-order precision in time while including a compact spatial discretization methodology to provide high-order spatial accuracy. The governing equations of electrokinetically driven non-Newtonian flows exhibit nonlinearity and coupling, which our hybrid framework efficiently manages. A computational scheme has been proposed for solving time-dependent partial differential equations. The proposed scheme was second-order accurate, and a compact scheme was presented for handling space-dependent terms. The numerical findings verify that the suggested method can seize the complex behaviour of electro-osmotic flow in non-Newtonian fluids. Particularly, it was noted that the velocity profile rises with increased Helmholtz-Smoluchowski velocity and electro-osmotic parameters. The effect of rheological characteristics and electrokinetic forces was also correctly depicted, proving the created approach's accuracy and dependability. The compact scheme provided high-order accuracy in space. The stability and convergence of the scheme have also been provided. The concluding points can be stated in the following way:

- By increasing the electrical parameter, the velocity profile increased.
- The velocity profile declined by raising Weissenberg's number.

- An increase in the electro-osmotic parameter and the Helmholtz-Smoluchowski velocity resulted in a steeper velocity profile.
- The temperature profile showed behaviour by raising the Prandtl number.

This study offers a strong and quick computational tool for simulating complicated electro-osmotic flows in Carreau fluids. Easily expanded to additional non-Newtonian models and geometrical configurations, the framework provides possible uses in industrial fluid management systems, biomedical engineering, and microfluidic device design.

Future research could extend this work by incorporating fluid-structure interaction, three-dimensional geometries, and multi-frequency electric field effects, often present in practical BioMEMS configurations. Additionally, experimental validation and integration with real-time control algorithms would further support the deployment of such models in innovative microfluidic systems.

Limitations of Existing Electro-Osmotic Flow Models: Even though there is more and more research on modelling electro-osmotic flow, there are still some major problems with the current methods, especially regarding non-Newtonian Carreau fluids. Much research uses Newtonian or power-law models to make the rheological behaviour easier to understand. These models don't do a good job of showing the shear-thinning and rate-dependent viscosity properties always present in Carreau fluids. In addition, most classical models only look at steady-state solutions and don't consider transient or oscillatory boundary conditions typical in lab-on-a-chip and BioMEMS devices. When using numerical methods, implicit schemes or linearization procedures are typically used. These can make the behaviour of non-linear solutions less accurate or make the calculations more difficult. Also, important physical processes like changing thermal conductivity, moving reactive species, and interacting with magnetic fields are ignored or looked at separately, making such models less useful in real-world electro-thermal microfluidic systems. These problems show the importance of having a strong, clear, and very accurate computational framework that can model the complex interactions of non-linear, transient, and multi-physical effects in Carreau fluid dynamics when electro-osmotic forces are present.

Acknowledgement: This research was supported by the Deanship of Scientific Research, Imam Mohammad Ibn Saud Islamic University (IMSIU), Saudi Arabia.

Funding Statement: This work was supported and funded by the Deanship of Scientific Research at Imam Mohammad Ibn Saud Islamic University (IMSIU) (grant number IMSIU-DDRSP2503).

Author Contributions: Conceptualization, methodology, and analysis, Yasir Nawaz; funding acquisition, Nabil Kerdid; investigation, Muhammad Shoaib Arif; methodology, Umer Farooq; project administration, Nabil Kerdid; resources, Umer Farooq; supervision, Muhammad Shoaib Arif; visualization, Nabil Kerdid; writing review and editing, Muhammad Shoaib Arif; proofreading and editing, Nabil Kerdid. All authors reviewed the results and approved the final version of the manuscript.

Availability of Data and Materials: The manuscript included all required data and the implementation of information.

Ethics Approval: Not applicable.

Conflicts of Interest: The authors declare no conflicts of interest to report regarding the present study.

Nomenclature

Symbol	Description
u^*, v^*	Dimensional velocity components in x^* and y^* directions
u, v	Dimensionless velocity components

T	Temperature of the fluid
C	Species concentration
C_∞	Ambient concentration
T_w	Wall temperature
C_w	Wall concentration
t^*	Dimensional time
y^*	Dimensional coordinate perpendicular to plate
x^*	Dimensional coordinate along the plate
g	Acceleration due to gravity
B_o	Magnetic field strength
σ	Electrical conductivity
\bar{b}	Forchheimer coefficient (non-Darcy resistance)
c_p	Specific heat capacity
D_B	Mass diffusion coefficient
$\varepsilon_1, \varepsilon_2$	Dimensionless thermal sensitivity parameters
D_a	Darcy number
M	Magnetic parameter
S_c	Schmidt number
N	Buoyancy ratio
m_e	Electro-osmotic parameter (related to EDL)
S_h	Local Sherwood number
θ	Dimensionless temperature
ϕ	Dimensionless concentration
t	Dimensionless time
y	Dimensionless vertical coordinate
Γ	Carreau fluid parameter
m	Power-law index in Carreau model
ν	Kinematic viscosity
ρ	Fluid density
μ	Dynamic viscosity
β_T	Coefficient of thermal expansion
β_c	Coefficient of solutal expansion
E_x	Applied electric field strength
k	Permeability of the porous medium
k_1	First-order chemical reaction rate constant
$K(T)$	Variable thermal conductivity
q'''	Internal volumetric heat generation
We	Weissenberg number (fluid elasticity)
F_s	Forchheimer number (inertial porous resistance)
Pr	Prandtl number
γ	Dimensionless reaction rate
U_{HS}	Helmholtz–Smoluchowski slip velocity
A^*, B^*	Heat generation/absorption coefficients

References

1. Liu M, Yang J. Electrokinetic effect of the endothelial glycocalyx layer on two-phase blood flow in small blood vessels. *Microvasc Res.* 2009;78(1):14–9. doi:10.1016/j.mvr.2009.04.002.
2. Minerick AR, Ostafin AE, Chang HC. Electrokinetic transport of red blood cells in microcapillaries. *Electrophoresis.* 2002;23(14):2165–73. doi:10.1002/1522-2683(200207)23:14<2165::AID-ELPS2165>3.0.CO;2-#.

3. Levine S, Marriott JR, Neale G, Epstein N. Theory of electrokinetic flow in fine cylindrical capillaries at high zeta-potentials. *J Colloid Interface Sci.* 1975;52(1):136–49. doi:10.1016/0021-9797(75)90310-0.
4. Misra JC, Chandra S, Shit GC, Kundu PK. Electroosmotic oscillatory flow of micropolar fluid in microchannels: application to dynamics of blood flow in microfluidic devices. *Appl Math Mech Engl Ed.* 2014;35(6):749–66. doi:10.1007/s10483-014-1827-6.
5. Jubery TZN. Modeling and simulation of electrokinetic manipulation of biological particles [Ph.D. thesis]. Pullman, WA, USA: Washington State University; 2012.
6. Dutta P, Beskok A, Warburton TC. Numerical simulation of mixed electroosmotic/pressure driven micro-flows. *Numer Heat Tran.* 2002;41:131–48 doi:10.1080/104077802317221366.
7. Jeffery GB. The two-dimensional steady motion of a viscous fluid. *Lond Edinb Dublin Philos Mag J Sci.* 1915;29(172):455–65. doi:10.1080/14786440408635327.
8. Hamel G. Spiralförmige bewegungen zäher flüssigkeiten. *Russ J Nonlinear Dyn.* 2009;5(1):111–33. (In German).
9. Ahmad S, Farooq M. Double-diffusive Hamel-Jeffrey flow of nanofluid in a convergent/divergent permeable medium under zero mass flux. *Sci Rep.* 2023;13(1):1102. doi:10.1038/s41598-023-27938-0.
10. Dinarvand S, Berrehal H, Tamim H, Sowmya G, Noeiaghdam S, Abdollahzadeh M. Squeezing flow of aqueous CNTs-Fe₃O₄ hybrid nanofluid through mass-based approach: effect of heat source/sink, nanoparticle shape, and an oblique magnetic field. *Results Eng.* 2023;17(1):100976. doi:10.1016/j.rineng.2023.100976.
11. Garimella SM, Anand M, Rajagopal KR. Jeffery-Hamel flow of a shear-thinning fluid that mimics the response of viscoplastic materials. *Int J Non-Linear Mech.* 2022;144(172):104084. doi:10.1016/j.ijnonlinmec.2022.104084.
12. Harley C, Momoniat E, Rajagopal KR. Reversal of flow of a non-Newtonian fluid in an expanding channel. *Int J Non-Linear Mech.* 2018;101(172):44–55. doi:10.1016/j.ijnonlinmec.2018.02.006.
13. Carreau PJ. Rheological equations from molecular network theories. *Trans Soc Rheol.* 1972;16(1):99–127. doi:10.1122/1.549276.
14. Khan SU, Ali Shehzad S. Analysis for time-dependent flow of Carreau nanofluid over an accelerating surface with gyrotactic microorganisms: model for extrusion systems. *Adv Mech Eng.* 2019;11(12):1687814019894455. doi:10.1177/1687814019894455.
15. Akbar NS, Nadeem S. Carreau fluid model for blood flow through a tapered artery with a stenosis. *Ain Shams Eng J.* 2014;5(4):1307–16. doi:10.1016/j.asej.2014.05.010.
16. Arif MS, Shatanawi W, Nawaz Y. A computational framework for electro-osmotic flow analysis in Carreau fluids using a hybrid numerical scheme. *Int J Thermofluids.* 2025;27:101240. doi:10.1016/j.ijft.2025.101240.
17. Arif MS, Shatanawi W, Nawaz Y. Stochastic analysis of electro-osmotic flow dynamics in porous media with energy dissipation. *Int J Thermofluids.* 2025;27(1):101172. doi:10.1016/j.ijft.2025.101172.
18. Hayat T, Saleem N, Mesloub S, Ali N. Magnetohydrodynamic flow of a carreau fluid in a channel with different wave forms. *Z Naturforsch A.* 2011;66a(9):215. doi:10.5560/zna.2011.66a0215.
19. Berrehal H, Dinarvand S, Khan I. Mass-based hybrid nanofluid model for entropy generation analysis of flow upon a convectively-warmed moving wedge. *Chin J Phys.* 2022;77(1):2603–16. doi:10.1016/j.cjph.2022.04.017.
20. Sochi T. Analytical solutions for the flow of Carreau and cross fluids in circular pipes and thin slits. *Rheol Acta.* 2015;54(8):745–56. doi:10.1007/s00397-015-0863-x.
21. Chaffin ST, Rees JM. Carreau fluid in a wall driven corner flow. *J Non Newton Fluid Mech.* 2018;253(6):16–26. doi:10.1016/j.jnnfm.2018.01.002.
22. Channakote MM, Marudappa S, Bég OA, Narayana M, Siddabasappa C. Electro-osmotic peristaltic streaming of a fractional second-grade viscoelastic nanofluid with single and multi-walled carbon nanotubes in a ciliated tube. *Results Eng.* 2025;26(3):104739. doi:10.1016/j.rineng.2025.104739.
23. Channakote MM, Shekar M, Dilipkumar VK. Electro-osmotic effect on peristaltic flow of phan-thien-tanner fluid in a planar channel. *ANZIAM J.* 2024;66(1):77–97. doi:10.1017/s1446181124000075.
24. Kumar P, Guruprasad MN, Almeida F. Thermal analysis of magnetized ZnO-blood nanofluid anticipating couple stresses in vertical microchannel using differential transform method. *J Mol Liq.* 2025;424(4):127051. doi:10.1016/j.molliq.2025.127051.

25. Kumar P, Vidhya KG, Almeida F, Al-Mdallal Q. Optimization using response surface methodology for Eyring-Powell fluid flow with Cattaneo-Christov heat flux and cross diffusion effects. *Int J Thermofluids*. 2025;25:100981. doi:10.1016/j.ijft.2024.100981.
26. Ahmed OS, Eldabe NT, Abou-zeid MY, El-kalaawy OH, Moawad SM. Numerical treatment and global error estimation for thermal electro-osmosis effect on non-Newtonian nanofluid flow with time periodic variations. *Sci Rep*. 2023;13(1):14788. doi:10.1038/s41598-023-41579-3.
27. Koç DA, Öztürk Y, Gülsu M. A numerical algorithm for solving one-dimensional parabolic convection-diffusion equation. *J Taibah Univ Sci*. 2023;17(1):2204808. doi:10.1080/16583655.2023.2204808.